nature communications

Article

https://doi.org/10.1038/s41467-024-53174-9

Simultaneous generation of residue-free reactive oxygen species and bacteria capture for efficient electrochemical water disinfection

Received: 25 February 2024

Accepted: 4 October 2024

Published online: 23 November 2024

Check for updates

Yong Liu[1,7], Lihao Wang[1,7], Qianhui Ma[1], Xingtao Xu[2] ✉, Xin Gao[1], Haiguang Zhu[1], Ting Feng[1], Xinyue Dou[1], Miharu Eguchi[3,4], Yusuke Yamauchi[4,5,6] ✉ & Xun Yuan[1] ✉

Residue-free and highly efficient techniques for drinking water disinfection are urgently needed. Herein, we report an electrochemical water disinfection system equipped with atomically precise Ag_{28} nanoclusters (NCs) as electrode materials. The deployment of these Ag_{28} NCs not only provides sufficient electrosorption sites for intelligent microbe enrichment but also ensures high-efficiency dual-mode microbial killing through the in situ electrocatalytic production of residue-free reactive oxygen species (ROS) and the inherent antimicrobial activity of Ag_{28} NCs. Moreover, the design of the system enables a cyclical "alive microbe capture–killing–dead microbe desorption" process for continuous water disinfection. On this basis, this water disinfection system is efficient against broad-spectrum microbes (with >99.99% antimicrobial activity), durable (with a performance reduction of only 0.75% over 40 cycles and 99.90% antimicrobial efficiency for over 5 h of continuous operation), versatile (i.e., other NCs can be used), scalable (with water productivity of 213.33 L h^{-1} m^{-2}), energy efficient (with a low energy consumption of 4.91 Wh m^{-3}; 1.04 Wh m^{-3} without the pumping cost) and applicable for various real water samples. This study may open new avenues for global water disinfection techniques.

The significance of drinking water security for sustaining civilization and maintaining human health cannot be overstated, given that 3.6 billion people worldwide currently face a shortage of safe drinking water, with this likely expanding to 5.7 billion by 2050[1,2]. Chlorination, UV irradiation, and ozonation are common water disinfection techniques used in industry[3,4]. However, these techniques suffer from either carcinogenic residues (e.g., toxic trihalomethanes, haloacetic acids, and bromate from chlorination) or low processing efficiency (e.g., UV and ozonation)[5]. Therefore, there is an urgent need to explore residue-free and highly efficient techniques for industrial use in drinking water disinfection.

Hydrogen peroxide (H_2O_2) and other reactive oxygen species (ROS)[6] are commonly used as residue-free and broad-spectrum disinfectants due to their strong oxidative ability, which leads to green

[1]School of Material Science and Engineering, Qingdao University of Science and Technology, Qingdao, China. [2]Marine Science and Technology College, Zhejiang Ocean University, Zhoushan, China. [3]School of Advanced Science and Engineering, Waseda University, Shinjuku, Tokyo, Japan. [4]Australian Institute for Bioengineering and Nanotechnology (AIBN), The University of Queensland, Brisbane, QLD, Australia. [5]Department of Materials Process Engineering, Graduate School of Engineering, Nagoya University, Nagoya, Aichi, Japan. [6]Department of Plant & Environmental New Resources, College of Life Sciences, Kyung Hee University, Yongin-si, South Korea. [7]These authors contributed equally: Yong Liu, Lihao Wang. ✉e-mail: xingtao.xu@zjou.edu.cn; y.yamauchi@uq.edu.au; yuanxun@qust.edu.cn

disinfection by the formation of oxygen and water[7,8]. Although the direct use of preformed H_2O_2 is a straightforward approach for water disinfection, it requires storage and transportation at the point of use and the use of stabilizers to prevent H_2O_2 degradation, with the side effect being lowering the antimicrobial efficacy of H_2O_2[9,10]. Thus, this method is inconvenient and inefficient. Alternatively, the catalytic in situ production of ROS by electrochemical or photochemical systems can overcome the drawbacks of preformed H_2O_2, with the electrocatalytic route being more advantageous than the photocatalytic one considering the poor penetration of light in water[11] and relatively slow photocatalytic kinetics[12]. For instance, Kim's group developed a series of self-powered (i.e., supercoiling-mediated rotational triboelectric nanogenerator) ROS-assisted electroporation disinfection systems with both nanowire-enhanced localized electric field and oxidative species to terminate the microbes and achieved high disinfection performance without additional energy input or disinfection byproducts[13,14]. However, current ROS-directed water disinfection techniques are limited by low disinfection efficiency, largely due to the spread of generated ROS into the bulk water stream[6]. Moreover, the requirements of such techniques in terms of the ultrahigh production of ROS and the ultrafast diffusion of ROS into bulk water streams made their practical application impossible[9]. This dilemma has raised two questions: What are the criteria for an ideal water disinfection technique? How can an excellent disinfection technique be designed? Deciphering the water disinfection process reveals six standards for an ideal technique: safe operation, no health risks, high efficiency, low cost, good durability, and adaptable decentralized application for underdeveloped regions. Developing a technique that meets several of these criteria is quite challenging, let alone fulfilling all of them simultaneously.

Regarding the design of an optimal water disinfection system, our hypothesis was that using an electrocatalytic ROS-directed water disinfection system with specific features would help us achieve this goal. We identified three essential features that the electrode material must possess: (i) efficient capture of microbes from the water stream using electrostatic interactions or other driving forces[15–19], ensuring that ROS and microbes encounter each other for efficient disinfection and avoiding the low disinfection efficiency caused by ROS diffusion; (ii) in situ production of ROS by the electrode material without damaging its catalytic activity or inherent antimicrobial properties, leading to the ultrahigh antimicrobial efficacy achieved by the high localized concentration of ROS and antimicrobial electrode materials; and (iii) avoidance of high-cost metals such as Au and Pd to keep the system affordable. Therefore, the key to realizing this optimal water disinfection method lies in the rational design of a multifunctional material that can fulfil the abovementioned criteria. Progress in the development of ultrasmall metal nanoclusters (NCs, <2 nm) presents an opportunity to design desirable electrode materials[20]. Metal NCs are novel functional nanomaterials with unique physicochemical properties, including atomically precise structures, tailorable surface chemistry, and molecule-like features such as strong luminescence, chirality, and HOMO–LUMO transitions[21–29]. For instance, precise Ag NCs can be used both as a model electrode material for the catalytic production of ROS for microbial killing and as intrinsic antimicrobial agents[20,30]. Configuring Ag NC-based electrode materials into an electrosorption device could ensure fast microbe capture for efficient water disinfection.

Herein, we present a capacitive-charging induced electrochemical water disinfection (CEWD) system that uses atomically precise $Ag_{28}(GSH)_{20}$ NCs as electrode materials (GSH denotes glutathione). These NCs are locked within the metal–organic framework (MOF) ZIF-67. This configuration not only improves the stability of $Ag_{28}(GSH)_{20}$ NCs but also provides sufficient electrosorption sites, which ensures high-efficiency dual-mode microbial killing through the in situ electrocatalytic production of ROS and the inherent antimicrobial activity of $Ag_{28}(GSH)_{20}$ NCs. In addition, the system design enables efficient capture of microbes in the bulk water stream onto the surface of the anode material, creating highly localized concentrations of ROS and microbes, as well as additional contact with antimicrobial electrodes for microbe killing. The system is broadly effective (>99.99% antimicrobial rate), ultrastable (an efficiency reduction of only 0.75% over 40 cycles), durable (99.90% bacterial killing efficiency for over 5 h of continuous operation), versatile (i.e., other NCs can be used), scalable (productivity of 213.33 L h m^{-2}), energy efficient (energy consumption of 1.04 Wh m^{-3}), and practicable. This work may provide a paradigm for the design of ROS-directed water disinfection systems featuring the electrocatalytic in situ formation of residue-free ROS with concurrent microbe capture through capacitive charging, which may promote the translation of this water disinfection technique in the water industry.

Results

Material characterizations

In this study, ultrasmall $Ag_{28}(GSH)_{20}$ NCs were selected as the electrocatalyst model and were further locked inside the framework of ZIF-67 for enhanced catalytic durability (denoted Ag NCs@ZIF-67). Afterwards, Ag NCs@ZIF-67 was assembled as the CEWD anode for highly efficient water disinfection based on the combined actions of the in situ production of residue-free ROS and concurrent microbe capture (Fig. 1).

Ag NCs@ZIF-67 synthesized via a two-step procedure (Fig. 2a). Specifically, $Ag_{28}(GSH)_{20}$ NCs were first prepared by a conventional $NaBH_4$ reduction method[31] and subsequently immobilized inside ZIF-

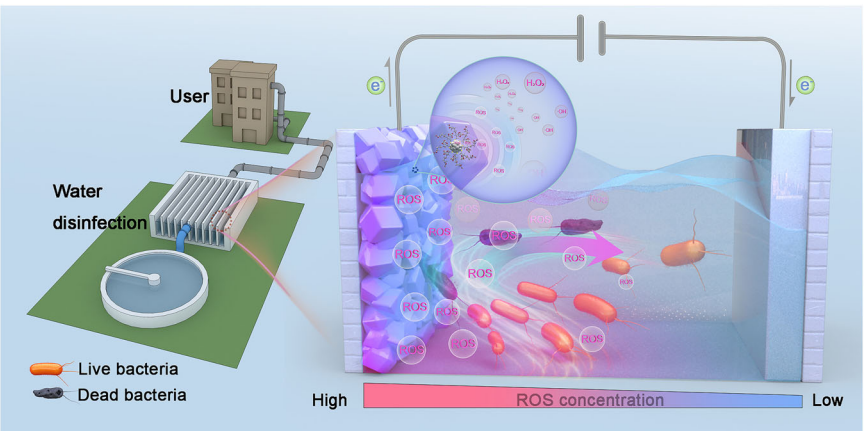

Fig. 1 | Schematic illustrations of CEWD. Schematic illustration of the application scenario and the working principle of CEWD for bacterial killing.

https://doi.org/10.1038/s41467-024-53174-9

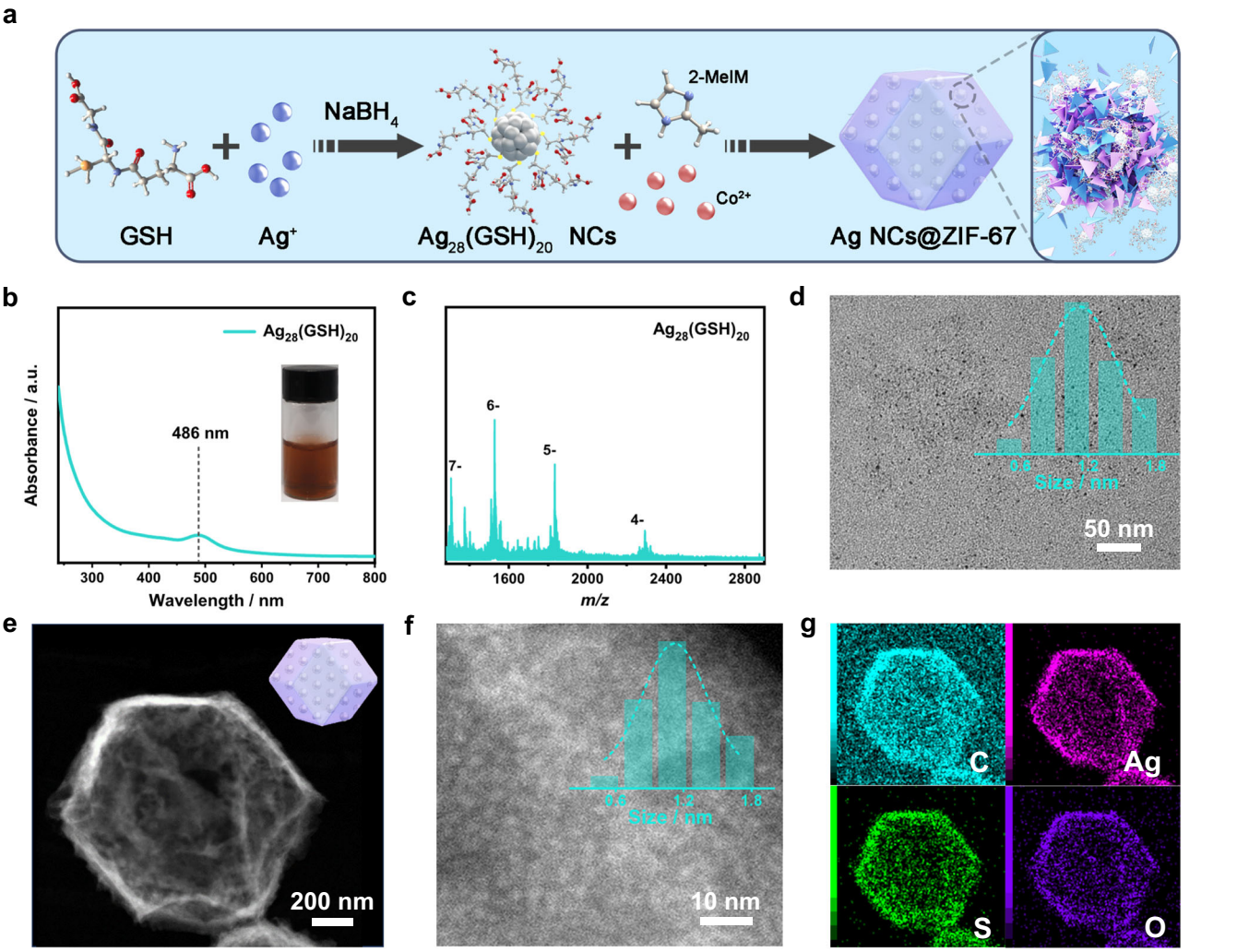

Fig. 2 | Structural characterizations of the $Ag_{28}(GSH)_{20}$ NCs and Ag NCs@ZIF-67. a Schematic illustration of the synthesis of Ag NCs@ZIF-67, **b** UV-vis absorption spectrum, **c** ESI-MS results, and **d** TEM image of $Ag_{28}(GSH)_{20}$ NCs; **e**–**f** HAADF-STEM images and **g** elemental maps (i.e. C, Ag, S, and O) of Ag NCs@ZIF-67. The insets in **b**, **d**, and **f** are digital photographs of $Ag_{28}(GSH)_{20}$ NC solutions under visible light, the particle size distribution of $Ag_{28}(GSH)_{20}$ NCs, and the particle size distribution of $Ag_{28}(GSH)_{20}$ NCs within ZIF-67, respectively.

67 via "coordination-assisted self-assembly"[32]. As the active component of Ag NCs@ZIF-67, $Ag_{28}(GSH)_{20}$ NCs were first characterized by UV-visible absorption spectrometry (UV-vis), electrospray ionization mass spectrometry (ESI-MS), and transmission electron microscopy (TEM). The UV-vis spectrum shows a dominant peak at 485 nm (Fig. 2b), indicating the formation of ultrasmall Ag NCs with molecule-like optical absorption. ESI-MS demonstrates peaks at m/z = 1305, 1527, 1834, and 2292, which correspond to the 7, 6, 5, and 4 charges of $Ag_{28}(GSH)_{20}$ NCs, respectively (Fig. 2c and Supplementary Fig. 1). The TEM image confirms the presence of ultrasmall Ag NCs with a core size of ~1.1 nm without the presence of large Ag nanoparticles (Fig. 2d).

$Ag_{28}(GSH)_{20}$ NCs were accommodated inside ZIF-67 to create Ag NCs@ZIF-67 (Fig. 2e). To highlight the advantages of the Ag NCs@ZIF-67 configuration, ZIF-67@Ag NCs was also prepared as a reference by in situ formation of Ag NCs on the surface of preformed ZIF-67 (Supplementary Fig. 2a). The size, morphology, and elemental distributions of both hybrids were examined using high-angle annular dark-field scanning transmission electron microscopy (HAADF-STEM) and TEM (Fig. 2e–g and Supplementary Fig. 2b–d). Figure 2e, f shows that in Ag NCs@ZIF-67, $Ag_{28}(GSH)_{20}$ NCs are uniformly embedded inside the ZIF-67 matrix without any change in size (inset of Fig. 2f), which was further supported by the X-ray diffraction (XRD) results (see Supplementary Fig. 3 and Supplementary Note I). This structure exhibits the catalytic activity of the $Ag_{28}(GSH)_{20}$ NCs, as ZIF-67 prevents aggregation and reinforces the structure with space confinement. In comparison, the morphology and size of the ZIF-67@Ag NCs (Supplementary Fig. 2b, c) are similar to those of the Ag NCs@ZIF-67.

Furthermore, the elemental maps of both Ag NCs@ZIF-67 and ZIF-67@Ag NCs confirm the uniform distribution of Ag and S throughout ZIF-67 (Fig. 2g and Supplementary Fig. 2d). Both hybrids have comparable loading amounts of Ag NCs, 2.90 wt% for Ag NCs@ZIF-67 and 2.87 wt% for ZIF-67@Ag NCs, as determined by inductively coupled plasma-mass spectrometry (ICP-MS). In addition, the oxidation states of Ag species in the Ag NCs and the Co species in the Ag NCs@ZIF-67 were also investigated by X-ray photoelectron spectroscopy (XPS, see Supplementary Figs. 4–6 and Supplementary Note I).

Disinfection evaluations

To assess the water disinfection efficiency, Ag NCs@ZIF-67 was assembled into a CEWD system as the anode (Fig. 3a) with surface-loaded ZIF-67@Ag NCs (right item on the right side of Fig. 3a) for comparison purposes. The CEWD system had an asymmetrical cell architecture and utilized activated carbon (AC) as the cathode. The configuration and parameters for the CEWD system are shown in Supplementary Fig. 7 and Supplementary Table 1. Before commencing

https://doi.org/10.1038/s41467-024-53174-9

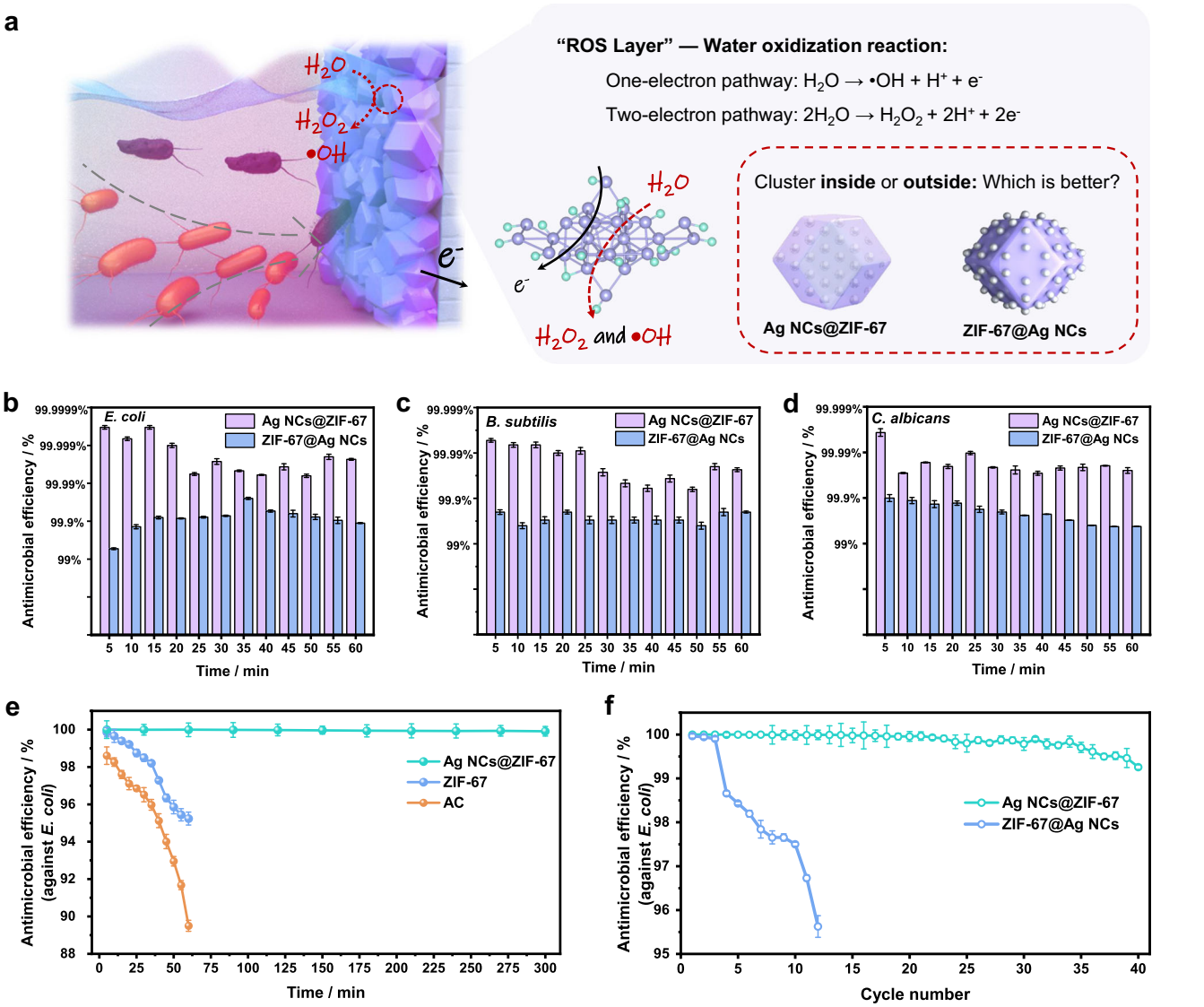

Fig. 3 | Disinfection evaluations of the Ag NCs@ZIF-67 and ZIF-67@Ag NCs-based CEWD systems. a Schematic illustration of the anode interface of the CEWD system for the electrocatalytic production of ROS for microbe killing and its key electrode components (Ag NCs@ZIF-67 and ZIF-67@Ag NCs); kill percentage against **b** *E. coli*, **c** *B. subtilis*, and **d** *C. albicans* achieved with Ag NCs@ZIF-67 and ZIF-67@Ag NCs-based CEWD during the first 60 min; **e** durability test performed on the AC, ZIF-67, and Ag NCs@ZIF-67-based CEWD systems against *E. coli* for 5 h; **f** long-term cyclic stability evaluation performed on the Ag NCs@ZIF-67 and ZIF-67@Ag NCs-based CEWD systems. Note: The feeding concentrations of *E. coli*, *B. subtilis*, and *C. albicans* were set to 10^6 CFU mL^{-1}. Error bars = s.d. ($n = 3$).

the water disinfection experiments, we optimized the loading amount of $Ag_{28}(GSH)_{20}$ NCs inside Ag NCs@ZIF-67 to 2.90 wt% and the operating voltage of the CEWD system to 1.4 V for experimentation, as shown in Supplementary Figs. 8–15. The model solution consisting of three typical microbes found in natural water sources, namely, gram-negative *E. coli* (abbreviated as *Escherichia coli*), gram-positive *B. subtilis* (abbreviated as *Bacillus subtilis)*, and the fungus *C. albicans* (abbreviated as *Candida albicans*), was pumped into the CEWD system through single-pass mode. As shown in Fig. 3b–d, Supplementary Fig. 11, and Supplementary Figs. 16–20, the Ag NCs@ZIF-67-based CEWD system displayed ultrahigh antimicrobial activity against all three microbes, with kill percentages of 99.99–99.9999% against *E. coli*, 99.90–99.999% against *B. subtilis*, and 99.90–99.999% against *C. albicans*, respectively. These antimicrobial activities were 1.86–2.2 orders of magnitude (based on log reduction) increment than that of the ZIF-67@Ag NCs-based CEWD system (i.e., 99.80–99.96% against *E. coli*, 99.60–99.80% against *B. subtilis*, and 99.50–99.80% against *C. albicans*), highlighting the unique ability of $Ag_{28}(GSH)_{20}$ NCs within ZIF-67 to enhance antimicrobial efficiency.

Interestingly, we observed a significantly greater killing efficiency against *E. coli* than against *B. subtilis* and *C. albicans*, which should be due to the thinner cell membrane (see Supplementary Table 2), as well as the enhanced driving force for *E. coli* capture in the electric field due to its having a more negative ζ-potential than did its counterparts (*E. coli*: −55.9 mV; *B. subtilis*: −39.4 mV; and *C. albicans*: −35.6 mV, 10^6 CFU mL^{-1}; Supplementary Table 3). The detailed antimicrobial mechanisms are discussed later. Nevertheless, only a trace amount of Ag ions was detected in the effluent (3.350 μg L^{-1}, Supplementary Table 4), an amount that is much lower than the guideline value (100 μg L^{-1}) for drinking water reported by the World Health Organization (WHO). In contrast, a higher concentration of released Ag ions (20.650 μg L^{-1}, Supplementary Table 4) was detected in the effluent of the CEWD system equipped with surface-loaded ZIF-67@Ag NCs than in that of the Ag NCs@ZIF-67. These results demonstrate that our strategy of embedding $Ag_{28}(GSH)_{20}$ NCs inside ZIF-67 can effectively protect $Ag_{28}(GSH)_{20}$ NCs from decomposition and prevent secondary water pollution without releasing Ag species into water.

Durability, cycling stability, and water safety are among the most important factors affecting the practical application of any water disinfection technique. Therefore, long-term (over 5 h) and multicycle (40 cycles) disinfection experiments were conducted (Fig. 3e–f and Supplementary Figs. 21–26). As shown in Fig. 3e, killing efficiency against *E. coli* of over 99.90% remains even after 5 h of continuous operation without any regeneration for our CEWD system, while the disinfection efficiency of the AC- and ZIF-67-based systems rapidly decreased to below 90% within 60 min. These results show the superior durability of the Ag NCs@ZIF-67-based CEWD system and its potential for continuous water disinfection in practical applications. Moreover, this outcome contradicts the "adsorption and termination" mechanism of conventional capacitive disinfection since the electrosorption equilibrium state should have long been reached (as seen in the AC-based system in Fig. 3e) and indicates that other dynamic processes must occur to trigger this ultradurable disinfection process, which is discussed in detail in the following section. Regarding cycling stability, only a 0.75% reduction (still greater than 99.90%) is found in the antimicrobial ratio for the Ag NCs@ZIF-67-based CEWD system after 40 disinfection/regeneration cycles (Fig. 3f and Supplementary Figs. 25–26), revealing its excellent cycling stability; however, the disinfection efficiency against *E. coli* with the ZIF-67@Ag NCs electrode rapidly decreases to below 99% within the first 5 cycles. This result was further supported by post-disinfection characterization using STEM, and ICP-MS. As shown, the structure of Ag NCs@ZIF-67 was well maintained after 40 disinfection/regeneration cycles (Supplementary Fig. 27), and the Ag content in Ag NCs@ZIF-67 barely changed according to the ICP-MS results (Supplementary Table 5), demonstrating the excellent structural stability of Ag NCs@ZIF-67. Moreover, the Ag content in the ZIF-67@Ag NCs decreased from 2.87% to 1.61% (Supplementary Table 5), and few Ag NCs were observed in the HAADF-STEM images of the ZIF-67@Ag NCs after cycling (Supplementary Fig. 28). These distinct differences demonstrate the effectiveness of encapsulating $Ag_{28}(GSH)_{20}$ NCs within ZIF-67 in improving their structural stability and ensuring their durability and cycling stability. Furthermore, the Ag NCs@ZIF-67-based CEWD system was confirmed to have excellent biocompatibility through the LIVE/DEAD viability assay and cell proliferation kit (MTT) test (Supplementary Figs. 29 and 30 and Supplementary Note II). This validation highlights the exceptional ability of these systems to ensure water safety.

Antimicrobial mechanism

The excellent water disinfection performance of the Ag NCs@ZIF-67-based CEWD system calls for further investigation of its antimicrobial mechanism. As depicted in Fig. 4a, the antimicrobial mechanism can be elaborated upon in three aspects. First, the $Ag_{28}(GSH)_{20}$ NCs in the electrode of the CEWD system first electrocatalytically generate abundant ROS in situ (see illustration in the upper right part of Fig. 3a)[33–36], forming a ROS layer for microbial killing (upper left part of Fig. 4a). These ROS are highly toxic to microbes, such as bacteria and fungi, triggering their effective elimination. The experimental findings demonstrated that these ROS were mainly produced at the anode of the CEWD system (Fig. 4b, Supplementary Figs. 31–34, and Supplementary Note III), with the majority being H_2O_2 (244.83 μM) and a minority being hydroxyl radicals (•OH, 3.39 μM). Although less •OH was produced than H_2O_2, •OH is known to possess 10^8 times greater antimicrobial activity than H_2O_2 and plays a crucial role in killing bacteria and fungi[9,37]. Consequently, the CEWD system, with its •OH production, exhibits superior antimicrobial capabilities compared to conventional catalytic H_2O_2 production-based systems.

Second, the CEWD system, as shown in Fig. 4a (lower left part), employs $Ag_{28}(GSH)_{20}$ NCs with inherent antimicrobial activity to enhance its antimicrobial activity on the anode surface. However, relying solely on in situ-generated ROS and the inherent antimicrobial property of $Ag_{28}(GSH)_{20}$ NCs is not sufficient for efficient water disinfection. This is because ROS are not easily accessible to microbes in the bulk stream, and the encapsulated $Ag_{28}(GSH)_{20}$ NCs cannot reach microbes in the bulk stream. Consequently, the diffusion of ROS from the electrode surface into the bulk stream for microbial killing is hampered by the sharp decrease in the ROS concentration gradient and the susceptibility of ROS to decomposition during the diffusion process. Fortunately, the CEWD system overcomes these challenges by utilizing electrostatic attraction to capture negatively charged microbes from the bulk stream onto the anode surface (right part of Fig. 4a). This strategy creates high local concentrations of both ROS and microbes near the anode surface, maximizing the antimicrobial efficiency of the in situ-produced ROS and $Ag_{28}(GSH)_{20}$ NCs on the anode surface of the CEWD system.

To confirm the microbial capture ability of the CEWD electrode materials, we tested the ζ-potentials of bacteria and fungi. Both bacteria and fungi had negative charges, with values of −55.9 mV for *E. coli*, −39.4 mV for *B. subtilis*, and −35.6 mV for *C. albicans* (Fig. 4c and Supplementary Table 3). The negative charge of the microbes facilitates the use of charge attraction in the CEWD system for microbial enrichment. Moreover, when microbes are effectively killed on the surface of the anode, their ζ-potentials change accordingly. In particular, the negative charges of dead microbes are significantly reduced (−42.0 mV for *E. coli*, −27.9 mV for *B. subtilis*, and −25.1 mV for *C. albicans*), which facilitates their detachment from the anode surface. A detailed discussion of the cyclic "alive microbe capture–killing–dead microbe desorption" mechanism on the electrode is presented in Supplementary Note IV (Supplementary Figs. 35–37). Furthermore, we examined the electrosorption behaviour of microbes on the electrode surface. As depicted in Fig. 4d, the Ag NCs@ZIF-67-based CEWD system demonstrated a high bacterial adsorption rate, reaching as high as 1×10^6 CFU min^{-1} (the detailed calculation method can be found in Supplementary Fig. 38 and Supplementary Note V). The absorption rate remained steady at 9.91×10^5 CFU min^{-1} even after 300 min of continuous operation, confirming our initial assumption that microbes can be continuously trapped on the anode surface of the Ag NCs@ZIF-67-based CEWD system. Notably, this result is in stark contrast to that of AC electrode- or pure ZIF-67-based CEWD systems, which exhibit a rapid decrease in microbial adsorption rate after 1 h despite having a much larger surface area for electrosorption (Fig. 4d). Such a drastic contrast contradicts the law of electrosorption equilibrium, further strengthening the evidence for a cyclical "alive microbe capture–killing–dead microbe desorption" process that sustains continuous water disinfection. This process ensures that the CEWD system has efficient yet long-term antimicrobial activity. Moreover, the real-time removal of pathogens was assessed by a LIVE/DEAD assay through inverted fluorescence microscopy to determine how quickly the pathogens were terminated. Specifically, the disinfection experiment was carried out for different durations (1 min, 2 min, 3 min, and 4 min), followed by short-circuiting of the device to flush out both live and dead bacteria. As shown in Supplementary Fig. 39a–f, 91.18%, 96.58%, 97.64%, and 98.15% of the bacteria were terminated at 1 min, 2 min, 3 min, and 4 min, respectively. Remarkably, the antimicrobial efficacy reached 91.18% in just 1 min, indicating the rapid disinfection capability of our CEWD system. The disinfection efficacy could be much greater (as shown in Supplementary Fig. 39g through the plate counting method) under real operational conditions (not short-circuited) since the bacteria could be trapped on the surface of the electrode through electrosorption and could subsequently enable a much longer time for termination. Taken together, the CEWD system achieves efficient microbial enrichment and subsequent water disinfection through the electrostatic capture of microbes, as well as in situ-produced ROS and the intrinsic antimicrobial activities of the $Ag_{28}(GSH)_{20}$ NCs[38], respectively.

Two interesting issues may arise: (1) Does the intrinsic antimicrobial activity of $Ag_{28}(GSH)_{20}$ NCs contribute to microbial killing

https://doi.org/10.1038/s41467-024-53174-9

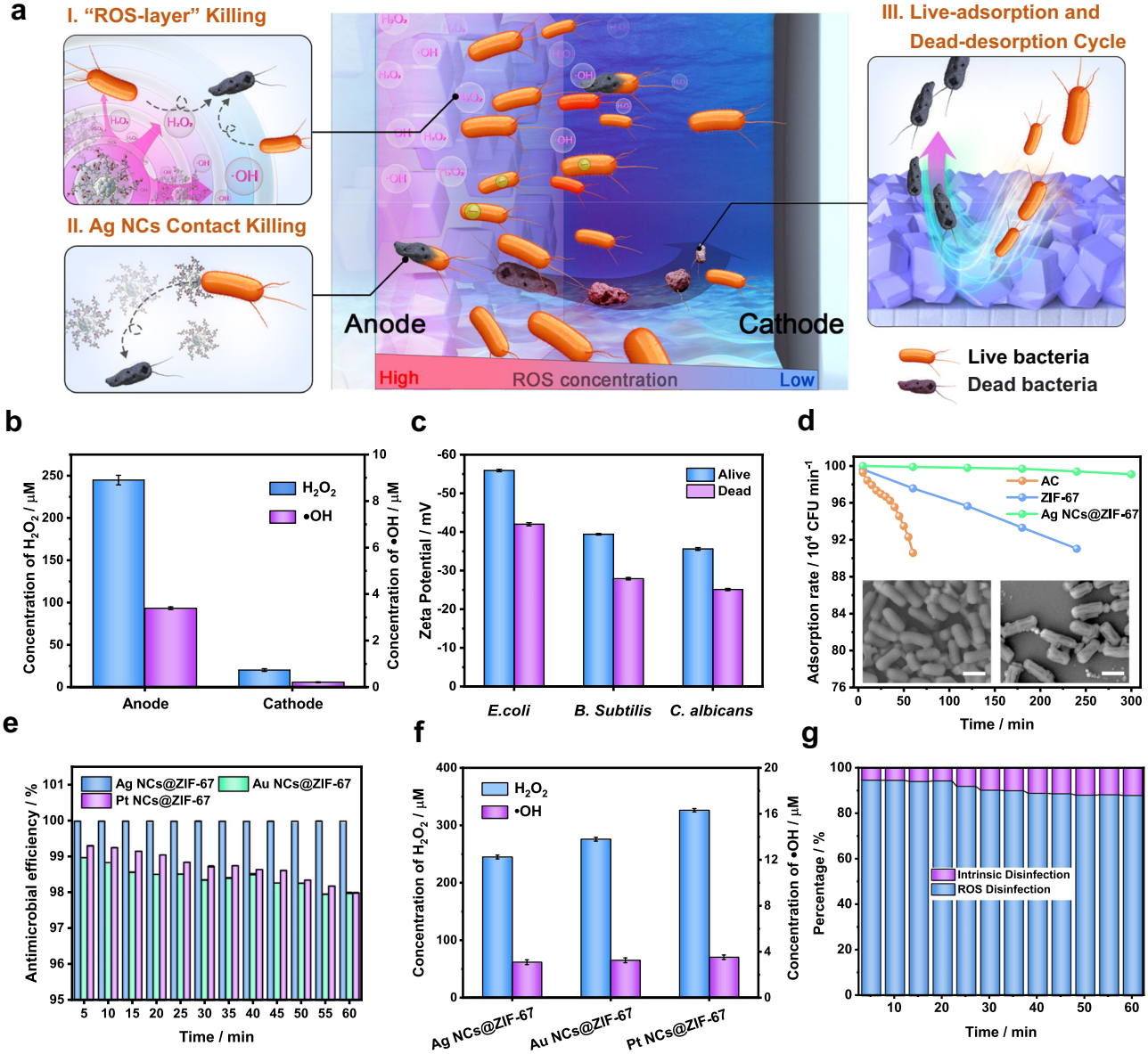

Fig. 4 | Antimicrobial mechanism explorations of the Ag NCs@ZIF-67-based CEWD system. a Schematic illustration of the water disinfection mechanism of the Ag NCs@ZIF-67-based CEWD system: (I) in situ production of ROS for microbial killing, (II) microbial killing by the $Ag_{28}(GSH)_{20}$ NCs with inherent antimicrobial activity, and (III) smart alive microbe capture–killing–dead microbe desorption circulation; **b** comparison of ROS (H_2O_2 and •OH) generation at the cathode and anode of the Ag NCs@ZIF-67-based CEWD system; **c** ζ-potentials of live and dead *E. coli*, *B. subtilis*, and *C. albicans*; **d** time-course bacteria adsorption rate of the Ag NCs@ZIF-67, ZIF-67, and AC-based CEWD systems; **e** disinfection efficiency and **f** ROS (H_2O_2 and •OH) production of Ag NCs@ZIF-67, Au NCs@ZIF-67, and Pt NCs@ZIF-67-based CEWD systems with a feeding *E. coli* concentration of 10^6 CFU min^{-1}; **g** contribution analysis of the intrinsic disinfection of Ag NCs and ROS disinfection of the Ag NCs@ZIF-67-based CEWD system. Error bars = s.d. ($n = 3$). The insets in Fig. 4d are the SEM images of live (left, scale bar: 100 nm) and dead (right, scale bar: 100 nm) *E. coli*.

via physical contact? (2) Can other metal NCs or other materials be used as CEWD electrodes for antimicrobial application? To validate these issues, two similar electrode materials (i.e., Au NCs@ZIF-67 and Pt NCs@ZIF-67 fabricated by encapsulating Au NCs and Pt NCs in ZIF-67), and one electrode equipped with non-metallic covalent organic framework (COF) were employed for water disinfection test (Supplementary Figs. 40–42). While the loading amounts of Au NCs and Pt NCs in the ZIF-67 were adjusted to be similar to that of Ag NCs inside the ZIF-67 (Supplementary Table 6), the loading amount of COF in the model COF electrode was optimized to make its ROS production level comparable to the Ag NCs@ZIF-67 one. As shown in Fig. 4e–f and Supplementary Fig. 43, the local ROS concentration of Ag NCs@ZIF-67-based CEWD was relatively lower than that of the Au NCs@ZIF-67- and Pt NCs@ZIF-67-based CEWD systems, and exactly comparable to that of the model COF-based CEWD system. However, Ag NCs@ZIF-67 displayed greater antimicrobial efficiency against *E. coli* than its three counterparts (Fig. 4e–f and Supplementary Figs. 44–46), indicating that physical contact between $Ag_{28}(GSH)_{20}$ NCs and microbes (intrinsic disinfection of Ag NCs) also plays an important role in enhancing the antimicrobial activity of the CEWD system. To confirm the physical contact between Ag NCs@ZIF-67 and the bacteria, scanning electron microscopy–energy dispersion spectrometry (SEM–EDS) was conducted to construct surface element maps of the Ag NCs@ZIF-67. The results, as depicted in Supplementary Fig. 47, revealed the presence of Ag on the surface of ZIF-67, suggesting that effective contact could be established between Ag NCs and the bacteria and confirming our hypothesis of a dual-mode disinfection mechanism. To analyse the contributions of ROS and the intrinsic disinfection of Ag NCs to the

total antimicrobial efficacy, the antimicrobial efficacy of the model COF electrode-based and Ag NCs@ZIF-67-based CEWD systems was specifically compared (Supplementary Fig. 48). The model COF electrode demonstrated the ability to eliminate ~90% of bacteria, which means that the ROS contributed ~90% antimicrobial efficacy in the Ag NCs@ZIF-67-based CEWD system because of the same amount and types of ROS production by the Ag NCs@ZIF-67. Accordingly, the intrinsic antimicrobial activity of Ag NCs was found to enhance the overall antimicrobial efficiency by an additional ~10% in the Ag NCs@ZIF-67-based CEWD system (Fig. 4g), since COF has negligible intrinsic disinfection properties in this scenario. Consequently, the predominant factor influencing the antimicrobial efficacy of CEWD is ROS, with the intrinsic disinfection of Ag NCs further enhancing the antimicrobial efficacy. The preliminary success of applying different metal NCs (e.g., Ag, Au, and Pt) and other nanomaterials (e.g., COF) as the core materials for CEWD has proven the versatility of this strategy. This could establish a universal platform for various oxidation-based applications (e.g., bacterial killing, selective microreactors, advanced oxidation).

Theoretical exploration

Why could Ag NCs@ZIF-67-based CEWD produce substantial amounts of ROS? This should be correlated with the molecular structure of the $Ag_{28}(GSH)_{20}$ NCs[39]. Therefore, we first optimized the structure of $Ag_{28}(GSH)_{20}$ NCs based on first-principles calculations via structural optimization, a static self-consistent field (SCF), density of state calculations, and charge calculations using VASP-6.1.0 via density functional theory (DFT). The cross-section of $Ag_{28}(GSH)_{20}$ NCs is shown in Fig. 5a. Specifically, $Ag_{28}(GSH)_{20}$ NCs contain an Ag_{20} core (Td symmetry with a geometric symmetry of D2h (Fig. 5a), capped by two Ag_3S_3 motifs (i.e., type i), two Ag_1S_1 motifs (i.e., type ii), and twelve S terminals (i.e., two S terminals of type iii and ten S terminals of type iv). Upon acquiring the structure and the wavefunction of the $Ag_{28}(GSH)_{20}$ NCs (Supplementary Fig. 49 and Supplementary Note VI), we searched for the GSH ligands on the $Ag_{28}(GSH)_{20}$ NCs to identify potential active absorption sites for water molecules to facilitate ROS production, considering the lowest free energy on the potential energy surface. Through this analysis, we identified a total of eight adsorption sites for water molecules (Fig. 5b). Additionally, we provided the atomic coordinate parameters of the water molecules adsorbed by $Ag_{28}(GSH)_{20}$ NCs in the Supplementary File, while the adsorption-free energies of each site are presented in Supplementary Table 7. Notably, sites #2, #4, and #8 have the lowest free energy among all the active sites, implying that they are the most likely active sites for adsorbing water molecules for water oxidation.

To explore the detailed water oxidation pathway for ROS production, we constructed energy maps of different water oxidation pathways at these three active sites (#2, #4, and #8), including one-electron (to generate •OH, $H_2O \rightarrow$ •OH + $H^+ + e^-$, Fig. 5c), two-electron (to generate H_2O_2, $2H_2O \rightarrow H_2O_2 + 2H^+ + 2e^-$, Fig. 5d), and four-electron (to generate O_2, $2H_2O \rightarrow O_2 + 4H^+ + 4e^-$, Fig. 5e)[40–42] routes. Among them, OH* can desorb from the active site to generate free •OH via the one-electron route (Fig. 5c)[43], yet the desorption of OH* requires excess energy to overcome the energy barrier of ~0.5–1.1 eV[37]. In addition, the two-electron oxidation of water to form H_2O_2 is thermodynamically favourable (Supplementary Fig. 50 and Supplementary Note VII) based on the following facts: (1) the active site first adsorbs a water molecule to generate OH*, and the decrease in free energy is approximately 1.1–1.5 eV; (2) OH* recombines with another water molecule to form H_2O_2, and the free energy further decreases in this step (Fig. 5d). For the four-electron oxygen evolution reaction (OER, Fig. 5e), the elementary OER steps include the formation of OH* by dissociative adsorption of H_2O molecules, the formation of O* by deprotonation of OH*, O* oxidation to OOH*, and O_2 formation and release. Obviously, the rate-determining step in the OER is O* oxidation to OOH*, which requires excess energy to overcome the energy barrier of ~0.62–0.94 eV. Therefore, the water molecules adsorbed on the active site preferentially undergo two-electron oxidation to generate H_2O_2 instead of one- or four-electron oxidation. To further verify that H_2O_2 is generated from H_2O through two-electron water oxidation, we repeated the ROS generation experiment in D_2O and conducted a 2H nuclear magnetic resonance (NMR ^2H) test to determine whether D_2O_2 could be generated. As shown in Supplementary Fig. 51, while D_2O shows a single peak at ~4.8 ppm in its NMR 2H spectrum, two obvious peaks at ~4.8 ppm and ~3.8 ppm were found in the NMR 2H spectrum of the reacted D_2O solution after electrocatalytic treatment. This result indicates that D_2O_2 was generated from the oxidation of D_2O molecules, confirming that the water molecules underwent a two-electron oxidation process to generate H_2O_2.

Practical application

Scalability, energy efficiency, and adaptability are three crucial factors that impact the practical application of water disinfection devices. Therefore, we conducted initial tests to assess the scalability and applicability of the Ag NCs@ZIF-67-based CEWD system (Fig. 6a–b). First, we investigated the flow rate tolerance of the CEWD modules by increasing the electrode size and examining the disinfection rate at various flow rates (1–100 mL min^{-1}; Fig. 6c). The results show that the disinfection rate decreases with increasing flow rate for all electrode sizes, but the largest module (with an electrode size of 281.25 cm^2) maintains a high disinfection rate of 99.90%, even at 100 mL min^{-1}. Additionally, the water productivity increased exponentially with increasing module size, reaching 213.33 L h^{-1} m^{-2} for the 281.25 cm^2 module (Fig. 6d). We also analysed the relationship between water productivity and energy consumption at various module sizes and found that energy consumption decreases exponentially with increasing productivity (Fig. 6e). The energy consumption of the module with size × 5 was 4.91 Wh m^{-3} (1.04 Wh m^{-3} without pumping cost), with corresponding water productivity of 213.33 L h^{-1} m^{-2}, demonstrating its excellent energy efficiency. The high energy efficiency of our system could be attributed to the precise targeting of microbes and the continuous operation mode. Specifically, unlike conventional ROS antimicrobial techniques that need to generate a large amount of ROS to release into the microbe stream (the current to generate such an amount of ROS would be high), our CEWD system could trap microbes on the surface of the anode, while only a high local ROS concentration is needed to kill bacteria. Therefore, the current for ROS generation could be largely reduced (the current transients are shown in Supplementary Fig. 52). Moreover, the operational energy cost (e.g., pumping cost) could be reduced since our CEWD system operates in continuous mode and no additional energy is required for its regeneration.

Building on this promising energy efficiency, we evaluated the disinfection performance of the CEWD system for various real water samples, including those from rivers, lakes, seas, and reservoirs (Fig. 6b). Notably, the real water samples analysed in this study contained a mixture of ions and organic pollutants, posing potential challenges to the disinfection performance of the CEWD system. Total organic carbon (TOC) levels in these samples were assessed before and after disinfection treatment (refer to Supplementary Table 8), indicating the effectiveness of the CEWD system in removing TOC. The reduction in TOC can be attributed to the oxidation facilitated by the ROS generated during the disinfection process. Impressively, our CEWD system demonstrated exceptional efficacy in eliminating pathogens, achieving a greater than 99.90% killing rate across all water samples containing TOC (Fig. 6f). In addition, no detectable disinfection byproducts (DBPs), such as carcinogenic residues, were found in the treated water samples, as indicated in Supplementary Table 9,

https://doi.org/10.1038/s41467-024-53174-9

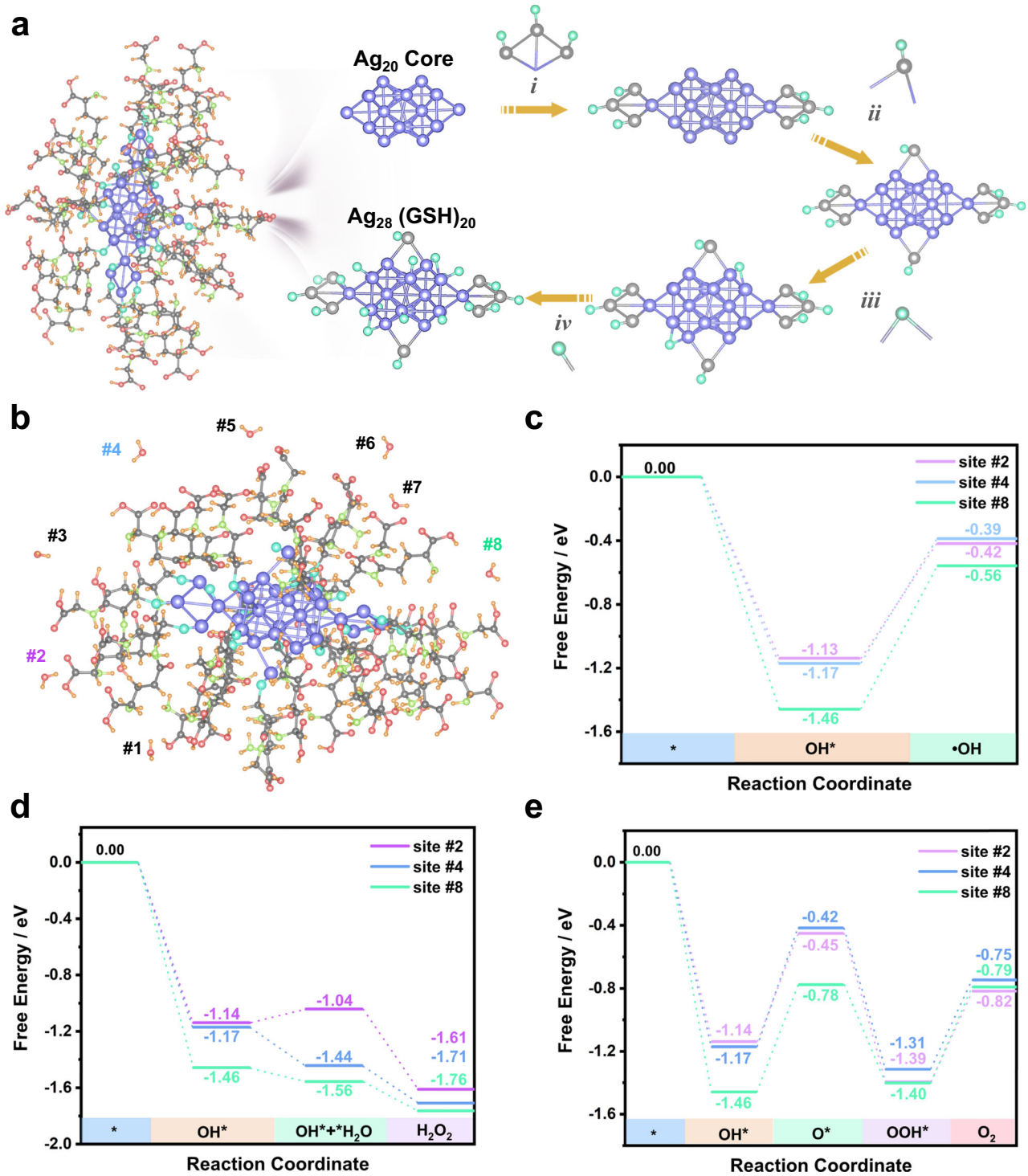

Fig. 5 | Theoretical exploration of the $Ag_{28}(GSH)_{20}$ NCs catalyst for ROS generation. a $Ag_{28}(GSH)_{20}$ NCs and its structural dissection. Colour codes: red = oxygen atom; white = hydrogen atom; dark blue = nitrogen atom; purple/grey = Ag atom; wathet blue = sulfur atom; black = carbon atom. **b** Active H_2O adsorption sites of $Ag_{28}(GSH)_{20}$ NCs; **c**–**e** free energy diagrams of •OH, H_2O_2, and O_2 production pathways on the active adsorption sites of $Ag_{28}(GSH)_{20}$ NCs.

underscoring the broad application scope, safety, and tolerance of the CEWD system to various salinity levels and organic pollutants (see Supplementary Figs. 53–54, Supplementary Table 10, Supplementary Movies 1–4, and Supplementary Note VIII). These results demonstrate that the CEWD system can adapt well to decentralized areas where water disinfection remains a great threat to public health but where large-scale water plants cannot be built, which is highly important for ensuring water security. Furthermore, we compared our CEWD system with other disinfection techniques from the literature, such as ex situ disinfection, UV, photocatalytic, and oxidation-assisted electroporation, in terms of energy utilization, safety, durability, disinfection efficiency, operability, and water flux (Fig. 6g and Supplementary Table 11). Our CEWD system exhibited outstanding disinfection performance without apparent limitations, demonstrating its potential for practical applications.

In summary, we designed a CEWD system equipped with an atomically precise $Ag_{28}(GSH)_{20}$ NC electrode for water disinfection. By integrating the in situ ROS production and the inherent antimicrobial

https://doi.org/10.1038/s41467-024-53174-9

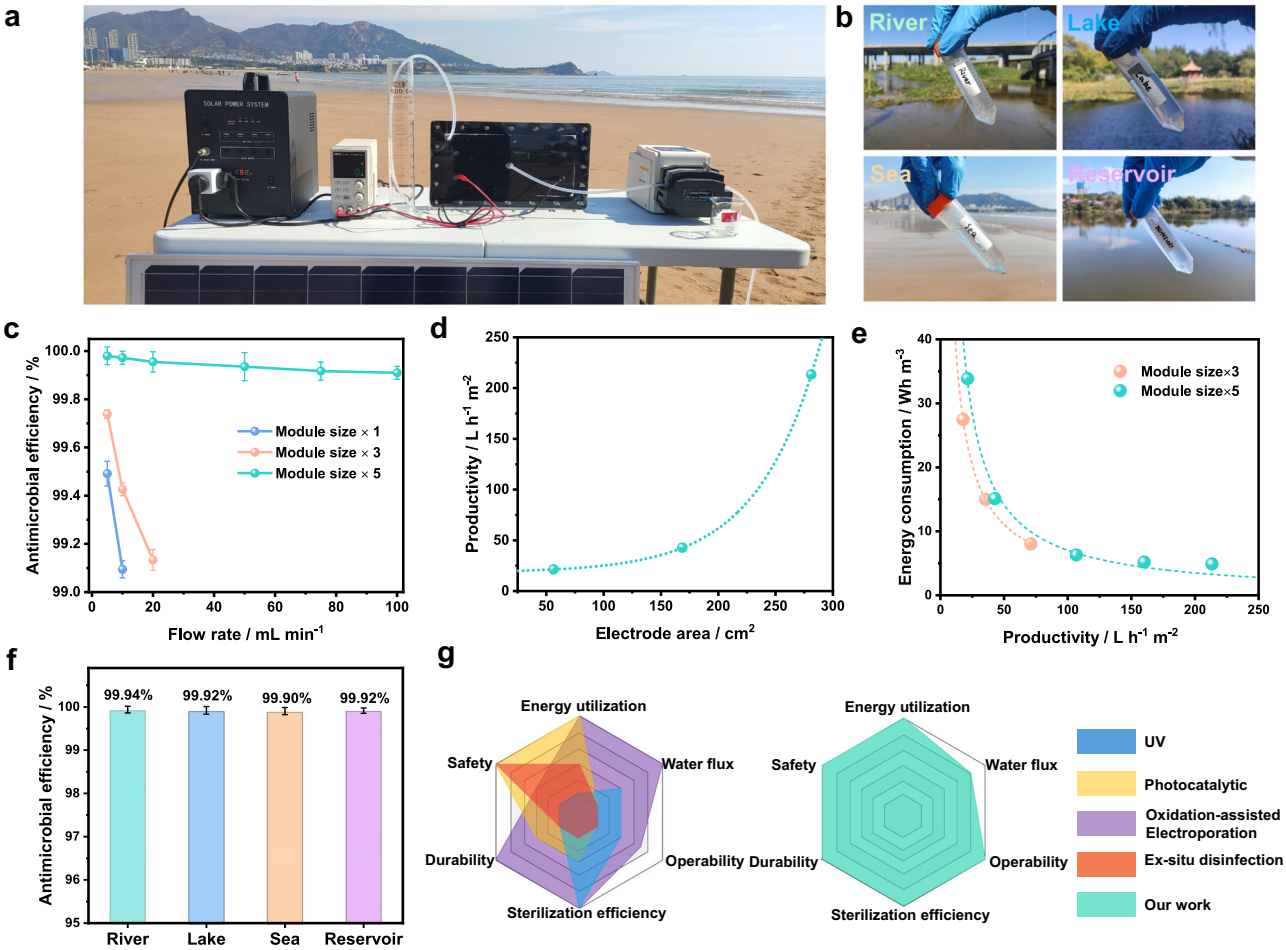

Fig. 6 | Scalability, energy efficiency, and adaptability evaluations of the CEWD system. Digital photos of **a** the practical-scale testing setup of the Ag NCs@ZIF-67-based CEWD system (the solar panel is used to provide electricity only) and **b** water samples collected from four natural sources; **c** maximum allowable flow rate of the three devices assuming that the antimicrobial efficiency is greater than 99.0%; **d** relationship between the maximum water productivity of the CEWD system and the electrode area; **e** energy consumption of the CEWD system as a function of water productivity; **f** antimicrobial performance of the CEWD system for four water samples; and **g** radar charts of the CEWD system in comparison with other water disinfection techniques in the literature[7,45–47]. Error bars = s.d. ($n = 3$).

activity of $Ag_{28}(GSH)_{20}$ NCs with smart microbe capture on the electrode surface, this water disinfection system was efficient against broad-spectrum microbes (with a >99.99% antimicrobial rate), ultra-stable (with only a 0.75% efficiency reduction over 40 cycles), durable (with 99.90% antimicrobial efficiency for over 5 h of continuous operation), versatile (i.e., other NCs can be used), scalable (with water productivity of 213.33 L h m^{-2}), energy efficient (with a low energy consumption of 4.91 Wh m^{-3}; 1.04 Wh m^{-3} without the pumping cost), and practically applicable for various real water samples. The brilliance of this study is the concurrent in situ formation of a high local ROS concentration via electrocatalysis and the inherent antimicrobial activity of Ag species with intelligent microbe enrichment on the electrode surface; ultimately, a continuous, highly efficient, and safe water disinfection strategy was established, which could provide new possibilities for global water hygiene.

Methods

Synthesis of $Ag_{28}(GSH)_{20}$ NCs

Reduced L-glutathione (GSH, 375 µL, 20 mM) and $AgNO_3$ (125 µL, 20 mM) were added to deionized (DI) water (4.4 mL) with vigorous stirring at room temperature to form an Ag(I)–GSH complex solution. Then, freshly prepared $NaBH_4$ (50 µL, ~112 mM) was added dropwise to the Ag(I)–GSH complex solution to form a deep-red clear solution, and the solution was then incubated at room temperature for ~3 h until the solution became colourless. Next, $NaBH_4$ (50 µL, ~112 mM) was added to the solution with stirring for 30 min and then aged at room temperature for 7 h. Finally, monodisperse $Ag_{28}(GSH)_{20}$ NCs were obtained by purifying the as-synthesized solution with a PD-10 desalting column, and the concentration of the $Ag_{28}(GSH)_{20}$ NCs was adjusted to 5 mM through rotary evaporation.

Synthesis of ZIF-67

The 2-methylimidazole (2-MeIM) was added to a $(CH_3COO)_2Co{\bullet}4H_2O$ solution with a Co^{2+} to 2-MeIM molar ratio of 1:40 under vigorous stirring at room temperature for 6 h. Then, the solution was aged at room temperature for 12 h. The resulting material was centrifuged (8000 rpm), washed repeatedly with DI water, and dried under vacuum at 80 °C for 48 h.

Synthesis of Ag NCs@ZIF-67

2-MeIM and $(CH_3COO)_2Co{\bullet}4H_2O$ (molar ratio: 37:1) were added to the as-synthesized $Ag_{28}(GSH)_{20}$ NC solution with a Co^{2+} to Ag^{+} molar ratio of 8:1 under vigorous stirring at room temperature for 6 h. Then, the solution was aged at room temperature for 12 h. The resultant precipitate was centrifuged (8000 rpm), washed with DI water, and dried under vacuum at 30 °C for 72 h.

Synthesis of ZIF-67@Ag NCs

GSH (375 µL, 20 mM), $AgNO_3$ (125 µL, 20 mM), and the as-synthesized ZIF-67 (5 mg) were added to 4.4 mL of DI water with vigorous stirring at

room temperature. Then, freshly prepared $NaBH_4$ (50 µL, ~112 mM) was added dropwise to the above solution for 5 min and aged at room temperature for 3 h. Afterwards, additional $NaBH_4$ (50 µL, ~112 mM) was added to the solution with stirring for 30 min, and the mixture was then aged at room temperature for 8 h. Finally, the ZIF-67@Ag NCs were obtained by centrifuging (8000 rpm), washing repeatedly with DI water, and drying under vacuum at 30 °C for 72 h.

Synthesis of $Au_{25}(GSH)_{18}$ NCs

$HAuCl_4$ (500 µL, 20 mM) and GSH (400 µL, 50 mM) were added to a mixed DI water (2.3 mL) and ethanol (6 mL) solvent with vigorous stirring at room temperature to form a GSH–Au(I) complex solution. Then, NaOH (200 µL, 1 M) and freshly prepared $NaBH_4$ (100 µL, ~112 mM) were added to the mixture with stirring for 3 h. Finally, the solution was centrifuged (8000 rpm) and redispersed in DI water to form a 5 mM $Au_{25}(GSH)_{18}$ NC solution.

Synthesis of GSH-protected Pt NCs

H_2PtCl_6 (200 µL, 100 mM) and GSH (400 µL, 50 mM) were added to DI water (9.5 mL) with vigorous stirring at room temperature to form the Pt(I)–GSH complex solution, and the pH of the solution was adjusted to 12.0 by adding NaOH (~150 µL, 1 M). Then, the Pt(I)–GSH complexes were reduced by bubbling CO into the solution for 5 min and sealing airtight with stirring for 24 h at room temperature. Finally, the concentration of the GSH-protected Pt NCs was adjusted to 5 mM through rotary evaporation.

Synthesis of COF

The 1,3,5-triformylphloroglucinol at a concentration of 0.30 mM and benzidine at 0.45 mM were each dissolved in 20 mL of ethanol. The resulting solutions were subsequently combined in a 100 mL flask and stirred at room temperature. After a stirring duration of 30 min, the resulting light brown suspension was subjected to centrifugation at 10,000 rpm for 5 min, followed by a thorough washing with ethanol. The resultant COF was refluxed with dimethylformamide (DMF) for 4 h to eliminate any unreacted residual, followed by a 2 h exchange with ethanol to replace the DMF. Ultimately, the synthesized COF was dried in a vacuum at room temperature overnight[44].

Detailed material characterizations, and antimicrobial evaluations are provided in the Supplementary Information.

Reporting summary

Further information on research design is available in the Nature Portfolio Reporting Summary linked to this article.

Data availability

Relevant data supporting the key findings of this study are available within the article and the Supplementary Information. All raw data generated during the current study are available from the corresponding authors upon request Source data are provided with this paper.

References

1. Alvarez, P. J. J., Chan, C. K., Elimelech, M., Halas, N. J. & Villagrán, D. Emerging opportunities for nanotechnology to enhance water security. *Nat. Nanotechnol.* **13**, 634 (2018).
2. He, C. et al. Future global urban water scarcity and potential solutions. *Nat. Commun.* **12**, 4667 (2021).
3. Shannon, M. A., Bohn, P. W., Elimelech, M., Georgiadis, J. G., Mariñas, B. J. & Mayes, A. M. Science and technology for water purification in the coming decades. *Nature* **452**, 301 (2008).
4. Jütte, M., Abdighahroudi, M. S., Waldminghaus, T., Lackner, S. & V. Lutze, H. Bacterial inactivation processes in water disinfection-mechanistic aspects of primary and secondary oxidants—a critical review. *Water Res.* **231**, 119626 (2023).
5. Mitch, W. A., Richardson, S. D., Zhang, X. & Gonsior, M. High-molecular-weight by-products of chlorine disinfection. *Nat. Water* **1**, 336 (2023).
6. Edwards, J. K. et al. Switching off hydrogen peroxide hydrogenation in the direct synthesis process. *Science* **323**, 1037 (2009).
7. Liu, C. et al. Rapid water disinfection using vertically aligned MoS_2 nanofilms and visible light. *Nat. Nanotechnol.* **11**, 1098 (2016).
8. Lin, Y.-J. et al. Thermocatalytic hydrogen peroxide generation and environmental disinfection by Bi_2Te_3 nanoplates. *Nat. Commun.* **12**, 180 (2021).
9. Richards, T. et al. A residue-free approach to water disinfection using catalytic in situ generation of reactive oxygen species. *Nat. Catal.* **4**, 575 (2021).
10. Xia, C., Xia, Y., Zhu, P., Fan, L. & Wang, H. Direct electrosynthesis of pure aqueous H_2O_2 solutions up to 20% by weight using a solid electrolyte. *Science* **366**, 226 (2019).
11. Fan, W. et al. Bactericidal efficiency and photochemical mechanisms of micro/nano bubble-enhanced visible light photocatalytic water disinfection. *Water Res.* **203**, 117531 (2021).
12. Bie, C., Wang, L. & Yu, J. Challenges for photocatalytic overall water splitting. *Chem* **8**, 1567 (2022).
13. Huo, Z.-Y. et al. Microbial disinfection with supercoiling capacitive triboelectric nanogenerator. *Adv. Energy Mater.* **12**, 2103680 (2022).
14. Huo, Z.-Y., Lee, D.-M., Wang, S., Kim, Y.-J. & Kim, S.-W. Emerging energy harvesting materials and devices for self-powered water disinfection. *Small Methods* **5**, 2100093 (2021).
15. Wang, Y. et al. High-performance capacitive deionization disinfection of water with graphene oxide-graft-quaternized chitosan nanohybrid electrode coating. *ACS Nano* **9**, 10142 (2015).
16. Kim, K. et al. Coupling nitrate capture with ammonia production through bifunctional redox-electrodes. *Nat. Commun.* **14**, 823 (2023).
17. Su, X., Kushima, A., Halliday, C., Zhou, J., Li, J. & Hatton, T. A. Electrochemically-mediated selective capture of heavy metal chromium and arsenic oxyanions from water. *Nat. Commun.* **9**, 4701 (2018).
18. Liu, Y. et al. In situ synthesis of bismuth nanoclusters within carbon nano-bundles from metal-organic framework for chloride-driven electrochemical deionization. *Adv. Funct. Mater.* **32**, 2110087 (2022).
19. Liu, X. et al. Unlocking enhanced capacitive deionization of $NaTi_2(PO_4)_3$/carbon materials by the yolk-shell design. *J. Am. Chem. Soc.* **145**, 9242 (2023).
20. Du, Y., Sheng, H., Astruc, D. & Zhu, M. Atomically precise noble metal nanoclusters as efficient catalysts: a bridge between structure and properties. *Chem. Rev.* **120**, 526 (2020).
21. Shi, W.-Q. et al. Near-unity NIR phosphorescent quantum yield from a room-temperature solvated metal nanocluster. *Science* **383**, 326 (2024).
22. Li, Y., Zhou, M., Song, Y., Higaki, T., Wang, H. & Jin, R. Double-helical assembly of heterodimeric nanoclusters into supercrystals. *Nature* **594**, 380 (2021).
23. Wang, X. et al. Ligand-protected metal nanoclusters as low-loss, highly polarized emitters for optical waveguides. *Science* **381**, 784 (2023).
24. Jia, T. et al. Eight-electron superatomic Cu_{31} nanocluster with chiral kernel and NIR-II emission. *J. Am. Chem. Soc.* **145**, 10355 (2023).
25. Yao, Q. et al. Supercrystal engineering of atomically precise gold nanoparticles promoted by surface dynamics. *Nat. Chem.* **15**, 230 (2023).
26. Narouz, M. R. et al. *N*-heterocyclic carbene-functionalized magic-number gold nanoclusters. *Nat. Chem.* **11**, 419 (2019).
27. Chen, J. et al. Atomically precise photothermal nanomachines. *Nat. Mater.* **23**, 271 (2024).

28. Zhang, H. et al. Bacteria photosensitized by intracellular gold nanoclusters for solar fuel production. *Nat. Nanotechnol.* **13**, 900 (2018).
29. Du, B. et al. Glomerular barrier behaves as an atomically precise bandpass filter in a sub-nanometre regime. *Nat. Nanotechnol.* **12**, 1096 (2017).
30. Yang, G., Wang, Z., Du, F., Jiang, F., Yuan, X. & Ying, J. Y. Ultrasmall coinage metal nanoclusters as promising theranostic probes for biomedical applications. *J. Am. Chem. Soc.* **145**, 11879 (2023).
31. Yuan, X., Setyawati, M. I., Tan, A. S., Ong, C. N., Leong, D. T. & Xie, J. Highly luminescent silver nanoclusters with tunable emissions: cyclic reduction-decomposition synthesis and antimicrobial properties. *NPG Asia Mater.* **5**, e39 (2013).
32. Luo, Y. et al. Fabrication of $Au_{25}(SG)_{18}$-ZIF-8 nanocomposites: a facile strategy to position $Au_{25}(SG)_{18}$ nanoclusters inside and outside ZIF-8. *Adv. Mater.* **30**, 1704576 (2018).
33. Tyo, E. C. & Vajda, S. Catalysis by clusters with precise numbers of atoms. *Nat. Nanotechnol.* **10**, 577 (2015).
34. Prieto, G., Zečević, J., Friedrich, H., de Jong, K. P. & de Jongh, P. E. Towards stable catalysts by controlling collective properties of supported metal nanoparticles. *Nat. Mater.* **12**, 34 (2013).
35. Hwang, G. B. et al. Photobactericidal activity activated by thiolated gold nanoclusters at low flux levels of white light. *Nat. Commun.* **11**, 1207 (2020).
36. Zheng, K. & Xie, J. Cluster materials as traceable antibacterial agents. *Acc. Mater. Res.* **2**, 1104 (2021).
37. Xie, J., Zhang, C. & Waite, T. D. Hydroxyl radicals in anodic oxidation systems: generation, identification and quantification. *Water Res.* **217**, 118425 (2022).
38. Zheng, K., Setyawati, M. I., Leong, D. T. & Xie, J. Antimicrobial silver nanomaterials. *Coordin. Chem. Rev.* **357**, 1 (2018).
39. Wang, J., Xu, F., Wang, Z.-Y., Zang, S.-Q. & Mak, T. C. W. Ligand-shell engineering of a Au_{28} nanocluster boosts electrocatalytic CO_2 reduction. *Angew. Chem. Internat. Edit.* **61**, e202207492 (2022).
40. Corby, S., Rao, R. R., Steier, L. & Durrant, J. R. The kinetics of metal oxide photoanodes from charge generation to catalysis. *Nat. Rev. Mater.* **6**, 1136 (2021).
41. Siahrostami, S. et al. Enabling direct H_2O_2 production through rational electrocatalyst design. *Nat. Mater.* **12**, 1137 (2013).
42. Okamura, M. et al. A pentanuclear iron catalyst designed for water oxidation. *Nature* **530**, 465 (2016).
43. Chen, Y.-C. et al. Electroactive membrane fusion-liposome for increased electron transfer to enhance radiodynamic therapy. *Nat. Nanotechnol.* **18**, 1492 (2023).
44. Yang, C., Liu, C., Cao, Y. & Yan, X. Facile room-temperature solution-phase synthesis of a spherical covalent organic framework for high-resolution chromatographic separation. *Chem. Commun.* **51**, 12254 (2015).
45. Murphy, H. M., Payne, S. J. & Gagnon, G. A. Sequential UV- and chlorine-based disinfection to mitigate *Escherichia coli* in drinking water biofilms. *Water Res.* **42**, 2083 (2008).
46. Liang, S., Lin, H., Habteselassie, M. & Huang, Q. Electrochemical inactivation of bacteria with a titanium sub-oxide reactive membrane. *Water Res.* **145**, 172 (2018).
47. Liu, H. et al. Carbon fiber-based flow-through electrode system (FES) for water disinfection via direct oxidation mechanism with a sequential reduction-oxidation process. *Environ. Sci. Technol.* **53**, 3238 (2019).

Acknowledgements

This work was supported by the National Natural Science Foundation of China (22478210, 52009057, 22071127, and 52301002), the Taishan Scholar Foundation of Shandong Province (tsqn201812074, China), Natural Science Foundation of Qingdao City (24-4-4-zrjj-184-jch), the China Postdoctoral Science Foundation (2023M731854), the Postdoctoral Science Foundation of Qingdao City (QDBSH20230101003), the JST-ERATO Yamauchi Materials Space-Tectonics project (JPMJER2003), the ES program (via Nagoya University), and the Australian Laureate Fellowship (FL230100095). This work used the Queensland node of the NCRIS-enabled Australian National Fabrication Facility (ANFF).

Author contributions

Y. Liu, L. Wang, Q. Ma, and Xin Gao performed the experiments and analysed the data. H. Zhu, T. Feng, and X. Dou repeated some antibacterial experiments. Y. Liu and X. Yuan conceived and supervised the project, and wrote the manuscript with insightful discussion and proofreading of X. Xu, M. Eguchi, and Y. Yamauchi. All authors have given approval to the final version of the manuscript. All authors discussed the results and commented on the article.

Competing interests

The authors declare no competing interests.

Additional information

Supplementary information The online version contains supplementary material available at https://doi.org/10.1038/s41467-024-53174-9.

Correspondence and requests for materials should be addressed to Xingtao Xu, Yusuke Yamauchi or Xun Yuan.

Peer review information *Nature Communications* thanks Sang-Woo Kim and Wanjun Wang for their contribution to the peer review of this work. A peer review file is available.

Reprints and permissions information is available at http://www.nature.com/reprints

Publisher's note Springer Nature remains neutral with regard to jurisdictional claims in published maps and institutional affiliations.

Open Access This article is licensed under a Creative Commons Attribution-NonCommercial-NoDerivatives 4.0 International License, which permits any non-commercial use, sharing, distribution and reproduction in any medium or format, as long as you give appropriate credit to the original author(s) and the source, provide a link to the Creative Commons licence, and indicate if you modified the licensed material. You do not have permission under this licence to share adapted material derived from this article or parts of it. The images or other third party material in this article are included in the article's Creative Commons licence, unless indicated otherwise in a credit line to the material. If material is not included in the article's Creative Commons licence and your intended use is not permitted by statutory regulation or exceeds the permitted use, you will need to obtain permission directly from the copyright holder. To view a copy of this licence, visit http://creativecommons.org/licenses/by-nc-nd/4.0/.

© The Author(s) 2024